The Astrophysical Journal, 646:1050–1058, 2006 August 1

VARIABILITY OF THE NGC 1333 IRAS 4A OUTFLOW: MOLECULAR HYDROGEN AND SILICON MONOXIDE IMAGES[1]

Minho Choi,[2] Klaus W. Hodapp,[3] Masahiko Hayashi,[4] Kentaro Motohara,[4,5] Soojong Pak,[2,6] and Tae-Soo Pyo[4]
Received 2006 January 31; accepted 2006 April 11

ABSTRACT

The NGC 1333 region was observed in the H_2 1–0 $S(1)$ line. The H_2 images cover a $5' \times 7'$ region around IRAS 4. Numerous H_2 emission features were detected. The northeast-southwest bipolar outflow driven by IRAS 4A was studied by combining the H_2 images with SiO maps published previously. The SiO-H_2 outflows are continuous on the southwestern side but show a gap on the northeastern side. The southwestern outflow lobe curves smoothly, and the position angle increases with the distance from the driving source. The base and the outer tip of the northeastern outflow lobe are located at positions opposite to the corresponding parts of the southwestern lobe. This point symmetry suggests that the outflow axis may be drifting or precessing clockwise in the plane of the sky and that the cause of the axis drift may be intrinsic to the outflow engine. The axis drift model is supported by the asymmetric lateral intensity profile of the SiO outflow. The axis drift rate is $\sim 0\overset{\circ}{.}011$ yr^{-1}. The middle part of the northeastern outflow does not exactly follow the point symmetry because of the superposition of two different kinds of directional variability: the axis drift of the driving source and the deflection by a dense core. The axis drift model provides a good explanation for the large deflection angle of the northeastern outflow. Other H_2 emission features around the IRAS 4 region are discussed briefly. Some of them are newly found outflows, and some are associated with outflows already known before.

Subject headings: ISM: individual (NGC 1333 IRAS 4) — ISM: jets and outflows — ISM: structure — stars: formation

1. INTRODUCTION

The NGC 1333 region contains numerous young stellar objects and outflows (Aspin et al. 1994; Hodapp & Ladd 1995; Rodríguez et al. 1999). It is one of the most active sites of star formation in the solar neighborhood, and the large number of active outflow sources was described as a "microburst" of star formation (Bally et al. 1996). Several protostars are located in the NGC 1333 molecular cloud, and IRAS 4A is one of the brightest submillimeter sources among them (Sandell & Knee 2001). IRAS 4A is a Class 0 protobinary system (Sandell et al. 1991; Lay et al. 1995; Looney et al. 2000).

Single-dish observations showed an interesting directional variability of the IRAS 4A molecular outflow (Blake et al. 1995). Detailed structure of the IRAS 4A molecular outflows within $\sim 1'$ of the driving source was revealed by interferometric observations. The interferometric maps showed that the apparently large change of outflow direction is partly owing to the existence of two outflows driven by IRAS 4A (Choi 2001b) and partly owing to the sharp bend (or deflection) in the northeastern lobe of the main bipolar outflow (Girart et al. 1999; Choi 2005a, hereafter Paper I). It was suggested in Paper I that the sharp bend was caused by a collision between the northeastern outflow and a dense core in the ambient molecular cloud. The jet-core collision model was supported by several lines of evidence, including the asymmetric morphology of the main outflow, the HCN emission from shocked high-density gas near the impact point, and the high-density core located in the course of the northeastern outflow (Paper I; Choi 2005b). However, the deflection cannot completely explain the difference of position angles between the SiO outflow near the driving source and the large-scale (>1′) CO/H_2 outflow.

To investigate the overall structure of the NGC 1333 IRAS 4A outflow system, we observed the outflows in several molecular tracers. In Paper I we presented high angular resolution observations in the SiO $v = 0$ $J = 1 \rightarrow 2$ line using the Very Large Array[7] (VLA). In this paper we present our observations in the H_2 1–0 $S(1)$ line using the University of Hawaii (UH) 2.2 m telescope and the Subaru Telescope. In § 2 we describe our H_2 observations. In § 3 we report the results of the H_2 imaging. In § 4 we compare the H_2 and the SiO images and discuss the variability of the IRAS 4A main outflow.

2. OBSERVATIONS

2.1. *UH* 2.2 m *Telescope Observations*

The molecular hydrogen emission features associated with IRAS 4 were included in a wide-field image of the NGC 1333 region in the H_2 1–0 $S(1)$ emission line obtained on the nights of 1996 July 30 to August 3 using the QUIRC camera (Hodapp et al. 1996) at the UH 2.2 m telescope. The individual integration time was 300 s. The image was produced by stepping the telescope in steps of 30″ in the north-south direction. Therefore, most positions in the image were covered by six individual frames for a total integration time of 30 minutes. In the overlap region between adjacent vertical stripes, the coverage is 12-fold for a total integration time of 60 minutes.

[1] Based in part on data collected at Subaru Telescope, which is operated by the National Astronomical Observatory of Japan.

[2] Korea Astronomy and Space Science Institute, Hwaam 61-1, Yuseong, Daejeon 305-348, South Korea; minho@kasi.re.kr.

[3] Institute for Astronomy, University of Hawaii, 640 North A'ohoku Place, Hilo, HI 96720; hodapp@ifa.hawaii.edu.

[4] Subaru Telescope, National Astronomical Observatory of Japan, 650 North A'ohoku Place, Hilo, HI 96720.

[5] Institute of Astronomy, University of Tokyo, Mitaka, Tokyo 181-0015, Japan.

[6] Department of Astronomy and Space Science, Kyung Hee University, Seocheon, Giheung, Yongin, Gyeonggi 446-701, South Korea.

[7] The National Radio Astronomy Observatory is a facility of the National Science Foundation operated under cooperative agreement by Associated Universities, Inc.

The UH H_2 image shows a set of artifacts that are the result of the residual excess dark current of the HgCdTe array used for the observations. This particular array, one of the earliest HAWAII-I devices, showed a strong excess of dark current in pixels previously exposed to high signal levels, with a decay time of the order of many minutes. As a result of this effect, combined with our method of collecting the individual images of this mosaic in a north-to-south stepping pattern, bright sources, most prominently SVS 13, are associated with a long string of residual images south of them, in 30″ spacing, and with slowly decaying intensity. The faint extended nebulosity discussed in this paper is not affected by this artifact.

2.2. *Subaru Telescope Observations*

Imaging was carried out on 2000 September 13 using the Cooled Infrared Spectrograph and Camera for OH-Airglow Suppressor (CISCO), which was equipped with a 1024×1024 HgCdTe detector covering a field of view of $110'' \times 110''$ with a plate scale of $0\farcs11$ pixel^{-1} (Motohara et al. 2002). We obtained narrowband images with and without H_2 1–0 $S(1)$ line emission. The H_2 1–0 filter was centered on $\lambda = 2.120$ μm with a width of 0.020 μm (FWHM), while the N215 filter for continuum emission was centered on 2.147 μm with a width of 0.021 μm (FWHM). Sixteen exposures of 60 s each were made for each of the filters by stepping the telescope in steps of $10''$–$20''$ along the east-west and/or north-south directions, resulting in the total on-source exposure time of 960 s for the central $90'' \times 90''$ region. Each frame of H_2 1–0 and N215 filter images was flat-fielded using sky-flat data and was subtracted by a corresponding sky frame, which was made for each of the two filters with median filtering. It was found that all of the extended features in the H_2 1–0 filter image arise from the H_2 1–0 $S(1)$ line by comparing it with the N215 filter image. We thus use only the H_2 1–0 filter image in this paper.

2.3. *Astrometric Calibration*

Accurate astrometry is essential to comparing the H_2 image with the SiO image. Since the adjacent continuum emission was not subtracted, the H_2 images include both the line and the continuum emission. In the UH H_2 image, 20 field stars listed in the Two Micron All Sky Survey (2MASS) Point Source Catalogue[8] were identified. In the Subaru H_2 image, only three 2MASS stars were found.

With the 2MASS coordinate data, the `geomap` package of IRAF was used to find the spatial transformation functions. Then the `geotran` package was used to transform the observed images. Comparing the stellar coordinates of the transformed UH H_2 image and of the 2MASS catalog, the rms of position difference is $0\farcs19$. This value is about the same order of the position uncertainties in the 2MASS catalog, which confirms that the transformation is acceptable.

Angular resolutions of the resulting images were measured by fitting Gaussian intensity profiles to stellar objects. The angular resolutions (FWHM) are $0\farcs82$ for the UH H_2 image and $0\farcs46$ for the Subaru H_2 image.

2.4. *VLA Data*

Details of the VLA observations and the results were presented in Paper I. The NGC 1333 IRAS 4 region was observed using VLA in the SiO $v = 0$ $J = 1 \rightarrow 2$ line. The resulting images have a restoring beam of FWHM $= 1\farcs96$. The SiO image covers a region up to $\sim 47''$ from IRAS 4A.

3. RESULTS

Figure 1 shows the UH H_2 image of the NGC 1333 cloud covering a $5\farcm2 \times 7\farcm5$ region. The Subaru H_2 image (Fig. 2) has a better sensitivity and a higher angular resolution than the UH image, but the field of view is smaller. In Figures 3*b* and 4*a*, the VLA SiO map of the IRAS 4A outflows is superposed on the H_2 images for comparison.

The structure of the H_2 emission features in the NGC 1333 region was previously discussed by Hodapp & Ladd (1995). Recent observations in the submillimeter and centimeter continuum (Rodríguez et al. 1999; Sandell & Knee 2001) provide helpful information for understanding the relation between the H_2 emission features and young stellar objects in this region. The NGC 1333 region is crowded with outflows, and the H_2 emission features should be inspected carefully to avoid confusion.

Since the main interest of this paper is the structure of the IRAS 4A molecular outflows, we describe the H_2 emission features related to these flows first. While the H_2 images show the large-scale structure of the main outflow, little H_2 emission can be seen near the driving source, probably owing to a high extinction through the dense core. In contrast, the SiO line nicely shows the outflow structure near the driving source, probably owing to a high density. Therefore, the H_2 images and the SiO map provide complementary information.

On the northeastern side, there is a relatively wide ($\sim 35''$) gap between ASR 57 and the northeastern end of the SiO outflow (Fig. 3*b*). This gap is probably real because CO outflow maps also show a similar gap (see Fig. 3 of Blake et al. 1995). A chain of H_2 features (ASR 57, HL 10, and HL 11=HH 347A) seems to belong to the IRAS 4A main outflow. Each of these features is elongated in the general direction of the flow. HH 347B is located away from the chain of H_2 features, and it probably does not belong to the IRAS 4A outflow.

On the southwestern side, the blueshifted SiO outflow is connected with the H_2 outflow, and there is a considerable overlap (Fig. 4*a*). Near the driving source, the faint H_2 feature CHH 15 coincides with SiO outflow peak (SiOOP) 7. The H_2 feature CHH 17 coincides with SiOOP 10 and 11 within a few arcseconds, and the northeastern end of CHH 18 coincides with SiOOP 12 (Fig. 4*a*). Farther away from the driving source, a chain of H_2 features (HL 5/3) seems to belong to the IRAS 4A main outflow.

Along the southern SiO outflow, the H_2 feature HL 6 is located in the middle of SiOOP 14, 15, and 16. Unlike the main outflow, the southern outflow shows no H_2 emission feature beyond the SiO outflow lobe. Therefore, the VLA SiO map probably traces the whole extent of the southern outflow.

3.1. *Proper Motion*

Proper motions of H_2 features were measured by comparing the Subaru and the UH images. The coordinate systems of the two images were aligned by comparing the positions of three stars near the H_2 features (ASR 53, ASR 103, and CHH 18 IRS). Since these stars are visible only in the near-IR or longer wavelengths, they are either stars embedded in the NGC 1333 molecular cloud or background stars, and their proper motions may be negligible. For bright H_2 features with well-defined peaks, position offsets were measured by comparing pixels around the peaks, typically pixels within $\sim 2''$ from the peak positions.

[8] This publication makes use of data products from the Two Micron All Sky Survey (2MASS), which is a joint project of the University of Massachusetts and the Infrared Processing and Analysis Center/California Institute of Technology, funded by the National Aeronautics and Space Administration and the National Science Foundation.

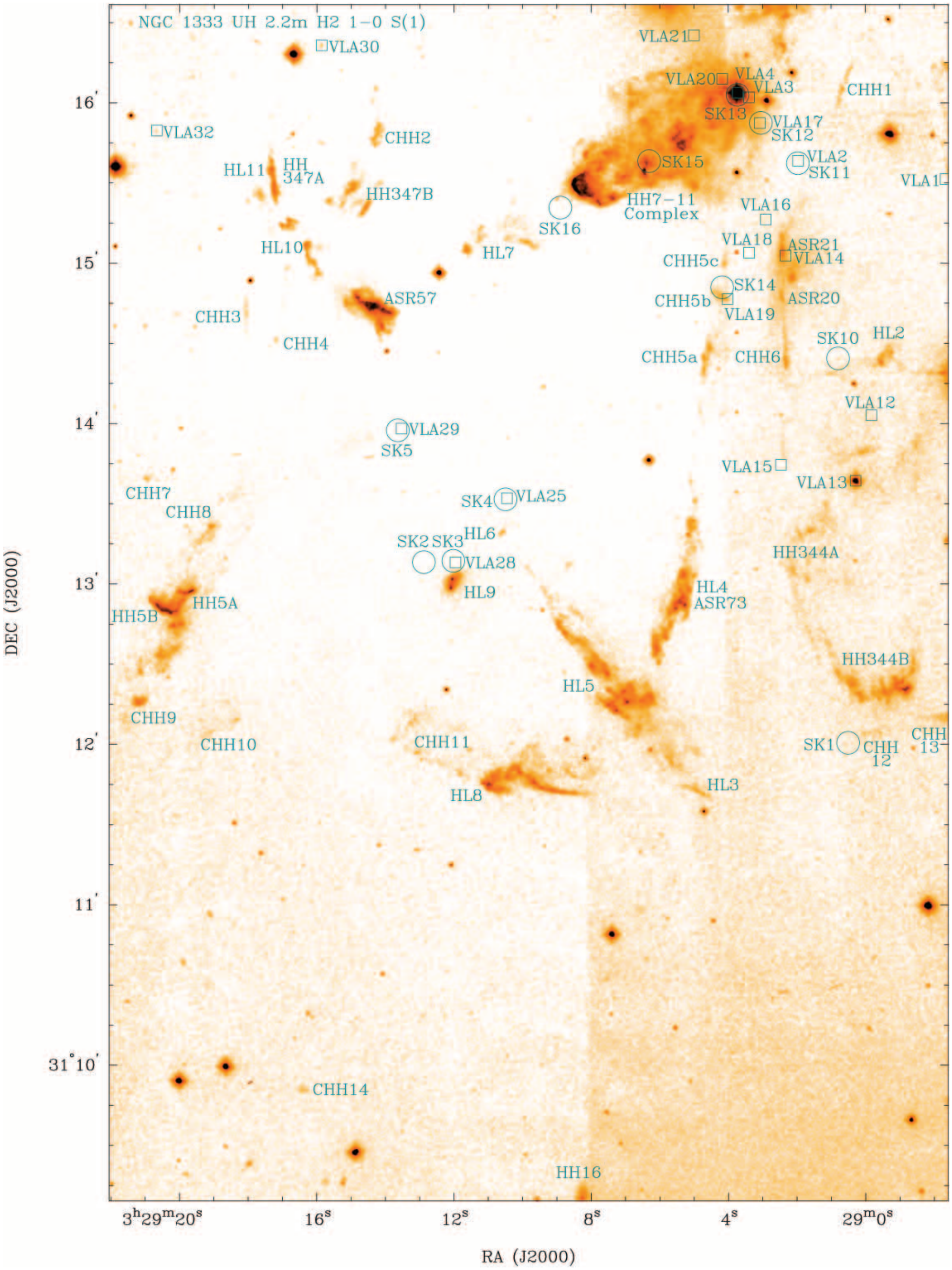

FIG. 1.—Map of the H_2 1–0 *S*(1) line toward the NGC 1333 IRAS 4 region from the UH 2.2 m telescope. Extended sources are labeled. HL source numbers are from Hodapp & Ladd (1995), ASR source numbers are from Aspin et al. (1994), and Herbig-Haro (HH) object numbers are from Bally et al. (1996 and references therein). Newly identified sources are numbered with a prefix CHH. *Squares*: Centimeter continuum sources labeled following Table 1 of Rodríguez et al. (1999). VLA 25 is associated with IRAS 4A, and VLA 4 is associated with SVS 13. *Open circles*: Submillimeter continuum sources labeled following Table 1 of Sandell & Knee (2001).

Additional measurements were made by comparing the Subaru image with the H_2 image of Hodapp & Ladd (1995) in a similar manner, which provides a longer time baseline but a larger uncertainty owing to the worse angular resolution. The two sets of measurements were consistent with each other, and the average proper-motion vectors are shown in Figure 5. The uncertainty of position offset was measured from the residual position differences of the five stars common to both images (the three stars above and ASR 54/55).

The proper-motion vectors of HL 4 peaks show a systematic motion toward southeast, and those of HL 5 peaks show a motion toward southwest. Assuming a distance of 320 pc (de Zeeuw et al. 1999), the proper motion of HL 5 peaks ranges from 30 to 120 km s^{-1} with an uncertainty of 50 km s^{-1}. In the discussions

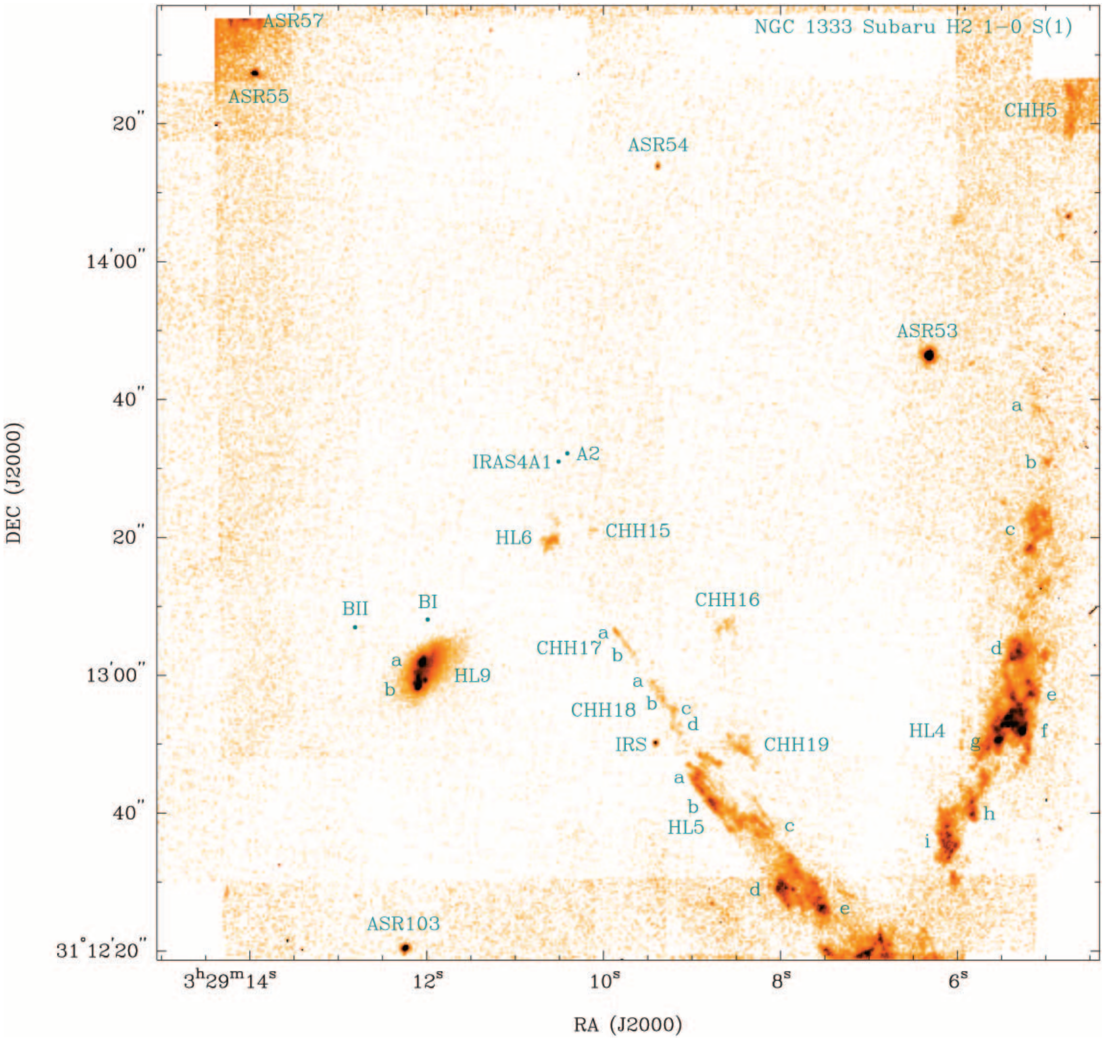

Fig. 2.—Map of the H_2 1–0 $S(1)$ line toward the NGC 1333 IRAS 4 region from the Subaru Telescope. Extended sources are labeled. *Filled circles*: Millimeter continuum sources in the IRAS 4 region (Looney et al. 2000).

below (§ 4), a proper motion of 100 km s^{-1} or 0.″07 yr^{-1} is assumed for calculations of the timescale of the IRAS 4A main outflow.

4. DISCUSSION

4.1. *Large-Scale Variability of the IRAS 4A Main Outflow*

As discussed in Paper I, the northeastern SiO outflow shows a directional variability that is probably caused by a collision with a dense core. On top of this variability, yet another directional variability is revealed by combining the SiO map with the H_2 images. This variability appears to affect both the southwestern and the northeastern outflows in a large (∼5′) scale. Since the northeastern outflow is more complicated owing to the superposition of the two different variabilities, we describe the southwestern outflow first.

The southwestern lobe of the SiO outflow appears very straight: all of the SiO outflow peaks are located within a beam size from a straight line (see Fig. 2*a* of Paper I). When the SiO and the H_2 images are superposed, however, the southwestern outflow appears to curve smoothly. That is, the position angle (P.A.) of the outflow peaks with respect to the driving source (IRAS 4A2) increases with the angular distance (Fig. 3*a*, *top panel*). Polynomial fits were drawn in Figure 3 to outline the flow. A change of flow direction can be caused either by intrinsic variability, such as geometric change of the outflow engine, or by external perturbation, such as density gradients in the external medium. The nearly constant gradient of the P.A.-distance relation suggests that the large-scale variability is probably owing to an intrinsic variability. Another important clue to the variability mechanism may come from the symmetry of the outflow morphology.

Near the driving source, the direction of the northeastern outflow is exactly opposite to that of the southwestern outflow. The northeastern outflow changes direction abruptly at a point ∼23″ away from the driving source, and the P.A. increases at a very high rate (Fig. 3*a*, *bottom panel*). At a large distance, however, the P.A.-distance relation converges back to the reverse of the southwestern flow. Therefore, it appears that the southwestern and the northeastern outflows would have shown a change of flow direction in a point-symmetric way, if it were not for the jet-core collision of the northeastern outflow. The symmetric morphology suggests that the change of flow direction in the large scale is caused by a geometric reconfiguration of the outflow engine. That is, the axis of the IRAS 4A2 accretion disk may be changing direction, and the outflow axis may be drifting[9]

[9] Outflows with changing directions are often described as "precessing." In this paper we use the term "drifting" instead of precessing because there is no evidence that the change is periodic.

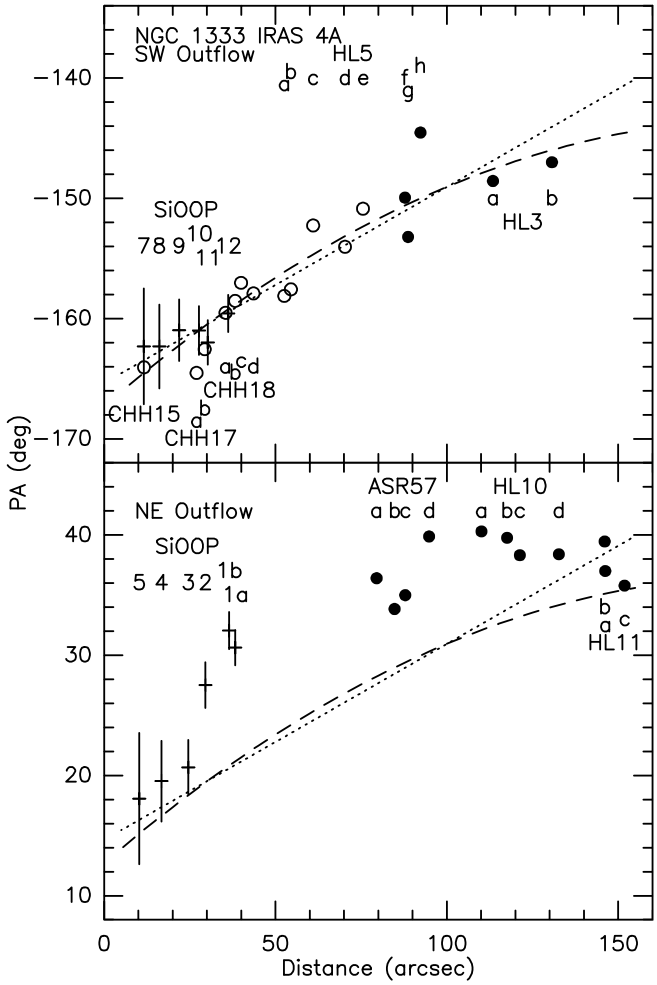

FIG. 3*a*

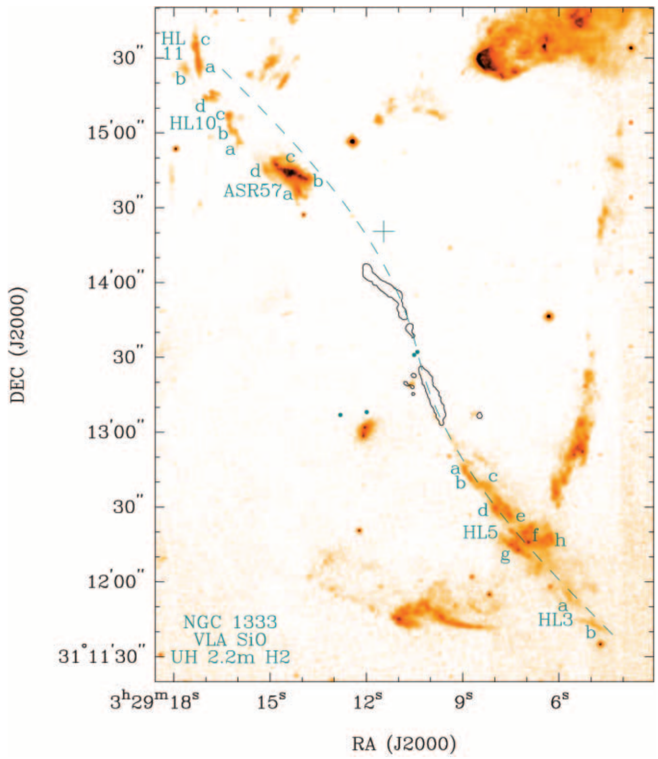

FIG. 3*b*

FIG. 3.—(*a*) P.A. of the emission peaks in the IRAS 4A main outflow plotted as a function of the angular distance with respect to the driving source (IRAS 4A2). *Top:* Southwestern outflow peaks. *Bottom:* Northeastern outflow peaks. *Plus signs:* SiO outflow peaks (Paper I; see Fig. 4). The vertical size corresponds to the beam (FWHM). *Open circles:* H_2 emission peaks identified in the Subaru image. *Filled circles:* H_2 emission peaks identified in the UH image. *Dotted line:* Linear least-squares fit to the southwestern outflow peaks. *Dashed line:* Parabolic least-squares fit to the southwestern outflow peaks. In the bottom panel, the fits in the top panel were drawn in reverse, i.e., with the P.A. shifted by 180°. (*b*) Maps of the H_2 line (*heat scale*) and the SiO line (*contours*) toward the NGC 1333 IRAS 4 region. The SiO map is the same as the one shown in Fig. 3*a* of Paper I. *Dashed line:* Parabolic fit in (*a*) drawn in the image coordinate. *Large plus sign:* HCO^+ peak position of the dense core obstructing the northeastern outflow (Choi 2005b). *Filled circles:* Millimeter continuum sources (Looney et al. 2000).

together. The axis appears to drift clockwise in the plane of the sky.

The IRAS 4A outflow is not the only example of a point-symmetric, or S-shaped, outflow driven by young stellar objects. Other examples include the HH 340/343 outflow driven by NGC 1333 J032845.3+310542 (K) and the H_2 jet driven by V380 Ori NE (Hodapp et al. 2005; Davis et al. 2000). Some outflows driven by high-mass (proto)stars appear to have similar shapes, e.g., IRAS 20126+4104 (Shepherd et al. 2000).

4.2. *Lateral Structure of the* SiO *Outflow*

The lateral structure of the SiO outflow was briefly described in § 3.3 of Paper I. Here we describe the structure in more detail and discuss it in the context of the drifting axis. Figure 4*b* shows the lateral intensity profiles. The SiO intensity profiles of the undeflected part of the main outflow (peaks 4–12) usually show a steep slope on the clockwise side and a relatively slower slope (or shoulder) on the counterclockwise side.

The asymmetric slopes of the intensity profiles can be explained by the drift of the flow axis. Since the axis of the primary jet drifts clockwise, the ambient molecular gas on the leading (clockwise) side would be relatively fresh (and probably denser), while the molecular gas on the opposite side would have been already disturbed and accelerated in the past. The shear zone between the primary jet and the ambient medium may be thinner on the leading side than on the trailing side. Then the SiO molecules in the shear zone of the leading side would be more strongly shocked, excited more highly, and make stronger emission, which could produce the asymmetric intensity profile across the outflow lobe. On the trailing side, the SiO-emitting gas may be gradually cooling down as the jet drifts away. Therefore, the asymmetric lateral intensity profile provides additional support for the drifting axis model.

4.3. *Drifting Axis of the IRAS 4A Main Outflow*

The P.A.-distance relation of the main outflow (Fig. 3*a*) suggests that the amount of axis drift within the observed extent of the main outflow (i.e., from the vicinity of the driving source to HL 3) is ~20° and that the rate of drift is ~10° $arcmin^{-1}$. Assuming a proper motion of 0.″07 yr^{-1} (see § 3.1), the temporal rate of axis drift is ~0.°011 yr^{-1}.

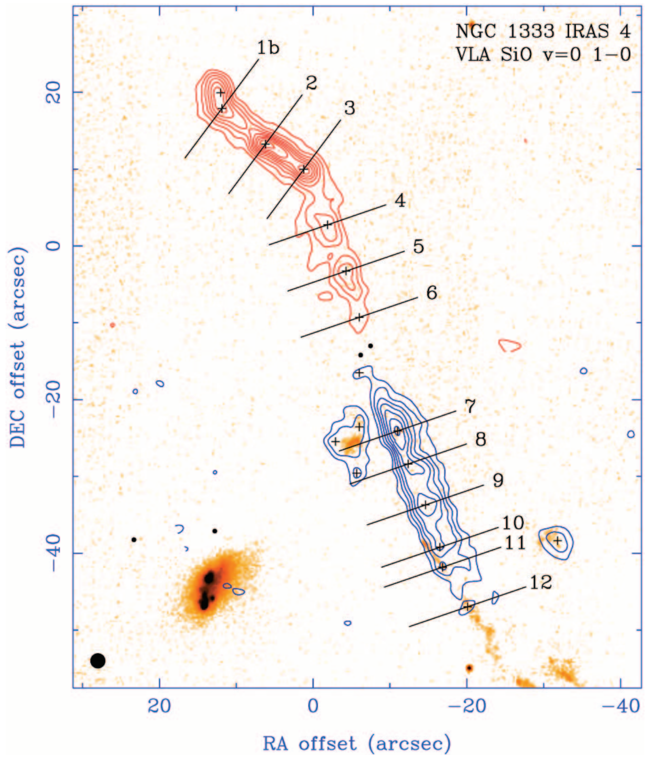

Fig. 4*a*

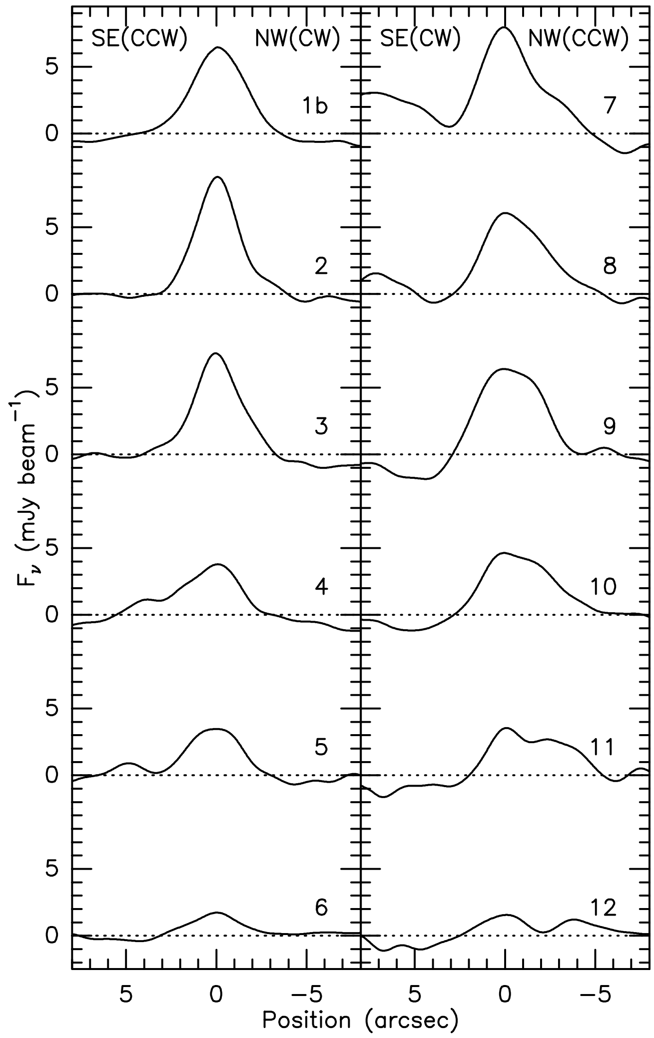

Fig. 4*b*

Fig. 4.—(*a*) Maps of the SiO line toward the NGC 1333 IRAS 4 region. See Figs. 2*a* and 6 of Paper I for details. Shown at the bottom left corner is the restoring beam: FWHM = $1''.96$. *Solid lines:* Cuts for the intensity profiles. They are perpendicular to the flow axis of the main bipolar outflow (the solid lines in Fig. 2*a* of Paper I). *Plus signs:* Peak positions of the SiO emission. Each peak of the main outflow is labeled at the end of the corresponding cut. *Heat scale:* H_2 line image from the Subaru Telescope (Fig. 2). (*b*) Intensity profile of the SiO emission across the outflow lobe. The narrow-line component in the southwestern region of the map is not included (see Paper I). The position axis is the angular distance along the cut in arcseconds from each SiO outflow peak position. The left edge of each panel corresponds to the southeastern end of the cut. In the northeastern outflow lobe (*left*), the clockwise side means the northwestern side. It is the other way around in the southwestern outflow lobe (*right*). The SiO peak number is labeled on the right side of each intensity profile.

Several authors suggested possible mechanisms of intrinsic outflow variability (e.g., Eislöffel & Mundt 1997; Fendt & Zinnecker 1998; Shepherd et al. 2000), but most of them cannot generate a large amount of drift as seen in the IRAS 4A outflow. The tidal interaction between IRAS 4A1 and IRAS 4A2 cannot explain the drift because the separation between them (>540 AU) is too large to cause a strong effect. In principle, A2 itself could be a close binary system that has not been observationally resolved yet. Assuming a proper motion of $0''.07$ yr^{-1}, the $130''$ separation between IRAS 4A and HL 3b gives an outflow timescale of ~2000 yr. Since the flow is not showing multiple turns, the precession period would be longer than 4000 yr, but it should be shorter than ~16,000 yr to keep the precession angle reasonably small, say, less than 90°. Since the precession period would be longer than the binary orbital period by a factor of ~20 (Bate et al. 2000), the expected orbital period of the unresolved binary system is 200–800 yr. The corresponding binary separation would be 30–80 AU, assuming that the mass of IRAS 4A2 is ~0.9 $M_\odot$, which is about half the mass of IRAS 4A (mass from Choi [2001b], scaled to 320 pc). Then the angular separation would be $0''.09$–$0''.25$, which is too small for existing millimeter interferometers to resolve. The accretion disk in such a system, however, would probably be too small to drive an energetic outflow.

Another possible mechanism is the anisotropic accretion that can occur when the angular momentum of currently accreting mass is not parallel to the rotation axis of previously accreted matter. Considering that IRAS 4A is a binary system, we propose the following scenario. The initial IRAS 4A core had fragmented into two subcores (A1 and A2), and each of them collapsed to form a protostar and started an outflow activity. While the total angular momentum of the A1/A2 system may be parallel to the rotation axis of the initial core, the spin axis of each individual protostar (and the initial direction of each outflow) could have been oriented differently. (This scenario is consistent with the observations because there is a considerable difference between

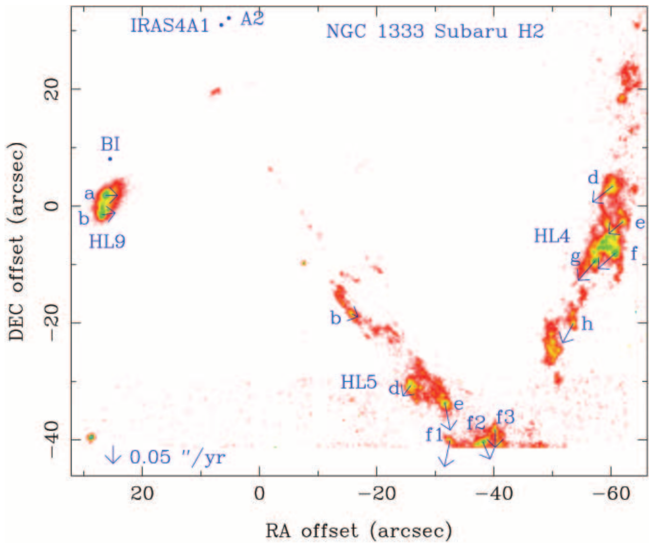

FIG. 5.—Proper-motion vectors superposed on the Subaru H_2 image. The length of arrows is proportional to the amount of proper motion, and the size of arrow heads corresponds to the uncertainty. The arrow at the bottom left corner shows the proper-motion scale.

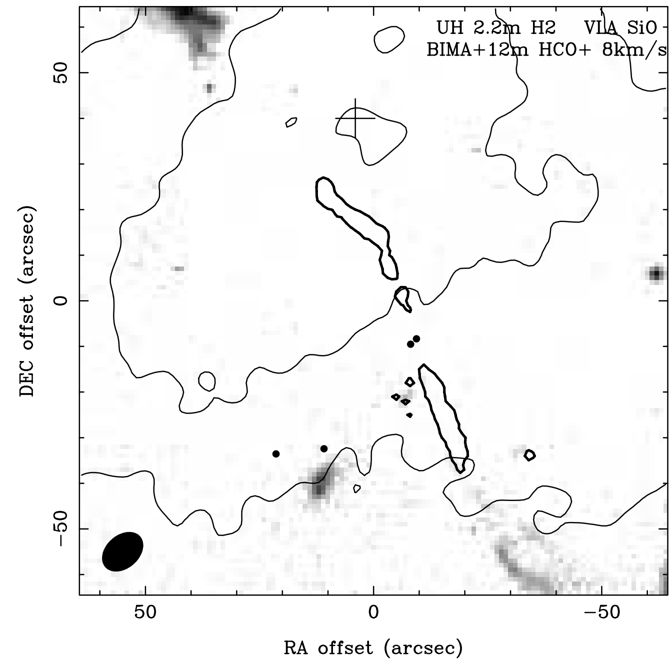

FIG. 6.—Maps of the H_2 line (*gray scale*), the SiO line (*thick contours*; Paper I), and the 8 km s^{-1} component of the HCO^+ $J = 1 \rightarrow 2$ line (*thin contours*; Choi 2005b). The HCO^+ and the SiO maps are not corrected for the primary beam response. Shown in the bottom left corner is the synthesized beam of the HCO^+ map. The markers are the same as those in Fig. 3*b*.

the directions of the main outflow driven by A2 and the southern outflow driven by A1.) As the protostar accumulates mass from the large outer envelope, the axis of the accretion disk would shift gradually and converge to the direction of the average angular momentum of the whole protostellar core. This scenario can be tested in principle by observationally determining the rotation axis of the IRAS 4A core, but the velocity structure of this region may be too complicated (Choi et al. 2004) for such a test. In the anisotropic accretion model, the change of direction may happen only once, i.e., may not be periodic or oscillating, which can explain why most of the direction-changing outflows observed so far do not show multiple turns.

Yet another possibility is the misalignment between the rotation and magnetic fields. Numerical simulations show that the rotation axis, magnetic fields, and disk orientation can precess significantly (Matsumoto & Tomisaka 2004). In such systems, changes of outflow direction may be observable. The evolution of the field direction with respect to the rotation axis may depend on the relative strength between the rotation and the magnetic fields (Machida et al. 2006).

4.4. *Deflection of the Northeastern Outflow*

Theoretical models of jet-cloud collision predict that, in the simple cases of steady jet, the deflection process finishes in a few hundred years either because the jet penetrates the dense clump or because the jet is pinched off (Raga & Cantó 1995; de Gouveia Dal Pino 1999). When the whole extent of the H_2 outflow is considered, the timescale of the IRAS 4A main outflow is ~2000 yr. Then the deflection process of a steady jet would have been almost finished in this timescale, and the deflection angle would have been small. The large deflection angle observed in the northeastern outflow suggests that the real situation is more complicated than the simple models. It was suggested that the deflection timescale can be longer if the jet beam is not steady so that the impact point does not stay at one position (Raga et al. 2002). Therefore, the drifting axis model provides a good explanation for the large deflection angle currently observed in the IRAS 4A outflow.

Assuming that the width of the (undeflected) primary jet at the impact point is smaller than 4″.3 (deconvolved width of SiOOP 4), and considering the axis drift rate in the previous section, it takes less than ~1000 yr for the impact point at the "surface" of the dense core to move across a jet width. Since this crossing time is comparable to or shorter than the cloud penetration timescale, the large deflection angle can be maintained.

The deflection history of the northeastern outflow can be summarized in the following scenario. Choi (2005b) suggested that the dense core obstructing the northeastern outflow is located ~50″ from IRAS 4A2 with a P.A. of ~16° (Figs. 3*b* and 6). The detection of HCO^+ and HCN emission suggests that the obstructing core is very dense (~10^5 cm^{-3}; Paper I; Choi 2005b). In the distant past, the direction of the outflow had a large position angle, and the flow would have passed by the eastern side of the obstructing core with a large impact parameter and would have been deflected only slightly. For example, HL 11 would have had a (projected) impact parameter of ~19″ (or 6000 AU at 320 pc). As the outflow axis drifts clockwise, the impact point would move on the "surface" of the dense core to the west, and the impact parameter decreases. Consequently, the outflow would be deflected more and more severely, and the deflection angle may increase with time. The P.A. of the outflow axis in the vicinity of the driving source is ~19°, and the jet currently colliding against the dense core may have an impact parameter of ~3″ or 900 AU. That is, the northeastern outflow is currently making a nearly head-on collision against the obstructing core, and consequently the deflection angle is large.

Reipurth et al. (1996) suggested that the HH 270/110 system may be an example of deflected outflow. This interpretation, however, was questioned because high-density molecular gas was not detected near the proposed impact point (Choi 2001a). Raga et al. (2002) suggested that the apparent conflict can be reconciled if the impact region is located far away from the crossing point of the

TABLE 1
H_2 Emission Features

Source	Peak Position	
	$\alpha_{J2000.0}$	$\delta_{J2000.0}$
CHH 1	03 29 00.7	31 16 05
CHH 2	03 29 14.3	31 15 47
CHH 3	03 29 18.1	31 14 42
CHH 4	03 29 17.2	31 14 31
CHH 5a	03 29 04.7	31 14 25
CHH 5b	03 29 04.1	31 14 46
CHH 5c	03 29 04.1	31 15 00
CHH 6	03 29 02.3	31 14 22
CHH 7	03 29 21.0	31 13 40
CHH 8	03 29 19.1	31 13 21
CHH 9	03 29 21.2	31 12 15
CHH 10	03 29 18.3	31 12 10
CHH 11	03 29 13.3	31 12 08
CHH 12	03 28 59.6	31 12 05
CHH 13[a]	03 28 57.6	31 12 09
CHH 14	03 29 16.4	31 09 51
CHH 15	03 29 10.1	31 13 21
CHH 16	03 29 08.7	31 13 07
CHH 17	03 29 09.9	31 13 06
CHH 18	03 29 09.3	31 12 56
CHH 19	03 29 08.5	31 12 49

Note.—Units of right ascension are hours, minutes, and seconds, and units of declination are degrees, arcminutes, and arcseconds.

[a] CHH 13 is at the edge of the field of view (Fig. 1). The actual peak position of CHH 13 may be located outside the region imaged.

HH 270 and the HH 110 axes. If the HH 110 flow is indeed a deflected segment of the HH 270 flow, its deflection history must be more complicated than the case of IRAS 4A. More detailed and sensitive observations are needed to understand the HH 270/110 system better.

4.5. *Other* H_2 *Emission Features*

The H_2 images (Figs. 1 and 2) show several emission features that were previously undetected or unlabeled. Coordinates of their peak positions are listed in Table 1. These H_2 features are labeled with a prefix CHH and briefly described here. Some of the previously known H_2 features are also discussed below.

CHH 1.—This is a short jetlike H_2 feature. A probable driving source is VLA 14.

CHH 2/4.—These H_2 features and HH 347B probably belong to a single outflow.

CHH 3.—This is a short jetlike H_2 feature. A probable driving source is ASR 74, the star just north of CHH 3.

CHH 5.—This is a linear chain of H_2 emission features. Hodapp & Ladd (1995) suggested that CHH 5 and HL 4 are related with the SVS 13 complex. Another possibility is that the CHH 5–HL 4 flow may be driven by VLA 19 (SK 14). Yet another possibility is that CHH 5b, which is elongated roughly in the northeast-southwest direction, may be a short outflow driven by VLA 19, while CHH 5a/c (and HL 4) may belong to a separate outflow.

CHH 6.—This is an unusually straight jetlike H_2 feature. It appears to be related with ASR 20/21 and probably with HH 344.

CHH 7/10/14.—These are isolated H_2 features with fuzzy appearances. Their nature is unclear. CHH 10 is associated with HH 759 (Walawender et al. 2005).

CHH 8/9.—These H_2 features seem to belong to the HH 5 system.

CHH 11.—This is a system of weak H_2 features. It appears to be related with HL 8.

CHH 12/13.—These H_2 features probably belong to a single outflow. A probable driving source is SK 1.

CHH 16.—This is a faint H_2 feature associated with SiOOP 17. Since SiOOP 17 is kinematically distinct from the IRAS 4A main outflow, it is not clear if it is related with the IRAS 4A system. See § 3.1 of Paper I for details.

CHH 19.—This H_2 feature probably belongs to the IRAS 4A outflow.

HL 8.—Hodapp & Ladd (1995) suggested that HL 8 may be an extension of HL 4. Considering the locations of SK 1 and CHH 12/13, however, HL 8 could be the counterpart of the CHH 12–13 outflow.

HL 9.—At $\sim 8''$ south of IRAS 4BI, the two peaks of HL 9 line up in the north-south direction, which agrees with the direction of the IRAS 4BI bipolar outflow seen in the HCN line (Choi 2001b).

ASR 57.—This is one of the brightest H_2 emission features in the region imaged. The location of ASR 57 at the intersection of the IRAS 4A outflow and the HH 7–11–HL 7 outflow raised the possibility that the two flows might be interacting (Hodapp & Ladd 1995). Since the dense core obstructing the IRAS 4A outflow is a part of the large cloud associated with SVS 13 and the HH 7–11 complex (Paper I; Choi 2005b), the two outflows may be close to each other along the line of sight. Further studies are needed to test whether or not they are physically interacting indeed. Proper-motion studies of the H_2 peaks within ASR 57 may be useful.

VLA 13/30/32.—These centimeter continuum sources were detected in the UH image as pointlike sources. The agreement between the VLA position and the near-IR position is good within $0\farcs2$.

We thank Mike Nassir for help with the reduction of the near-infrared image from the UH 2.2 m telescope. This work was partially supported by the LRG Program of KASI, by the Korea-Japan Basic Scientific Cooperation Program of KOSEF, and by the Japan-Korea Basic Scientific Cooperation Program of JSPS.

REFERENCES

Aspin, C., Sandell, G., & Russell, A. P. G. 1994, A&AS, 106, 165
Bally, J., Devine, D., & Reipurth, B. 1996, ApJ, 473, L49
Bate, M. R., Bonnell, I. A., Clarke, C. J., Lubow, S. H., Ogilvie, G. I., Pringle, J. E., & Tout, C. A. 2000, MNRAS, 317, 773
Blake, G. A., Sandell, G., van Dishoeck, E. F., Groesbeck, T. D., Mundy, L. G., & Aspin, C. 1995, ApJ, 441, 689
Choi, M. 2001a, ApJ, 550, 817
———. 2001b, ApJ, 553, 219
———. 2005a, ApJ, 630, 976 (Paper I)
———. 2005b, J. Korean Phys. Soc., 47, 533
Choi, M., Kamazaki, T., Tatematsu, K., & Panis, J.-F. 2004, ApJ, 617, 1157
Davis, C. J., Dent, W. R. F., Matthews, H. E., Coulson, I. M., & McCaughrean, M. J. 2000, MNRAS, 318, 952
de Gouveia Dal Pino, E. M. 1999, ApJ, 526, 862
de Zeeuw, P. T., Hoogerwerf, R., de Bruijne, J. H. J., Brown, A. G. A., & Blaauw, A. 1999, AJ, 117, 354
Eislöffel, J., & Mundt, R. 1997, AJ, 114, 280
Fendt, C., & Zinnecker, H. 1998, A&A, 334, 750
Girart, J. M., Crutcher, R. M., & Rao, R. 1999, ApJ, 525, L109
Hodapp, K. W., Bally, J., Eislöffel, J., & Davis, C. J. 2005, AJ, 129, 1580

Hodapp, K.-W., & Ladd, E. F. 1995, ApJ, 453, 715
Hodapp, K.-W., et al. 1996, NewA, 1, 177
Lay, O. P., Carlstrom, J. E., & Hills, R. E. 1995, ApJ, 452, L73
Looney, L. W., Mundy, L. G., & Welch, W. J. 2000, ApJ, 529, 477
Machida, M. N., Matsumoto, T., Hanawa, T., & Tomisaka, K. 2006, ApJ, 645, 1227
Matsumoto, T., & Tomisaka, K. 2004, ApJ, 616, 266
Motohara, K., et al. 2002, PASJ, 54, 315
Raga, A. C., & Cantó, J. 1995, Rev. Mex. AA, 31, 51
Raga, A. C., de Gouveia Dal Pino, E. M., Noriega-Crespo, A., Mininni, P. D., & Velázquez, P. F. 2002, A&A, 392, 267
Reipurth, B., Raga, A. C., & Heathcote, S. 1996, A&A, 311, 989
Rodríguez, L. F., Anglada, G., & Curiel, S. 1999, ApJS, 125, 427
Sandell, G., Aspin, C., Duncan, W. D., Russell, A. P. G., & Robson, E. I. 1991, ApJ, 376, L17
Sandell, G., & Knee, L. B. G. 2001, ApJ, 546, L49
Shepherd, D. S., Yu, K. C., Bally, J., & Testi, L. 2000, ApJ, 535, 833
Walawender, J., Bally, J., & Reipurth, B. 2005, AJ, 129, 2308